Enhanced optical, electrical, dielectric, and photovoltaic properties in strontium titanate by Ce-doping through a modified combustion method

Rini Varghese[1,2], Lakshmi J.S.[1,3], Steffy Maria Jose[1], Abraham A[4], JK Thomas[1*]

[1]Department of Physics, Mar Ivanios College (Autonomous), Thiruvananthapuram 695015, Kerala, India. [2] Department of Physics, St. Stephen's College, Pathanapuram 689695, Kerala, India. [3]Department of Science and Humanities, Mar Baselios College of Engineering and Technology, Thiruvananthapuram 695015, Kerala, India. [4]Department of Physics, Christian College, Chengannur, Kerala, India.

Article

Abstract

Structural, optical, electrical, dielectric and photovoltaic characteristics of cerium-doped strontium titanate was examined in this article. A set of single-phase compounds were created using a modified combustion process. Room temperature X-ray diffraction examination confirmed the

formation of a cubic phase in the Pm3m space group. The dimension of the crystallites increased after doping with cerium, according to HRTEM images. The FTIR spectra showed an indication of metal-oxide vibration-related peaks. Due to the introduction of midgap states with doping, the bandgap decreased with cerium infusion from x=0 to 0.03 as shown by UV-visible spectroscopy, raising the prospect of photovoltaic applications. In the dielectric characterization, the dielectric constant and loss of each compound showed an identical behavioral pattern: both were higher in the low-frequency region and rapidly decreased as frequency ascended until stabilizing. The dielectric constant in strontium titanate went up with A-site cerium doping in the perovskite strontium titanate. The loss factor increased for the cerium-doped sample in the low-frequency range and decreased in the mid-frequency region. The conductivity and frequency response of all materials followed Jonscher's power law. The total electrical conductivity increased in the doped samples. The electrical conductivity of the doped samples was improved by the reduction in activation energy brought on by doping. The electrical conductivity increased with temperature for all of the dense ceramics. The DSSC performs more effectively when utilizing a cerium-doped sample as the photoanode than when using an undoped sample.
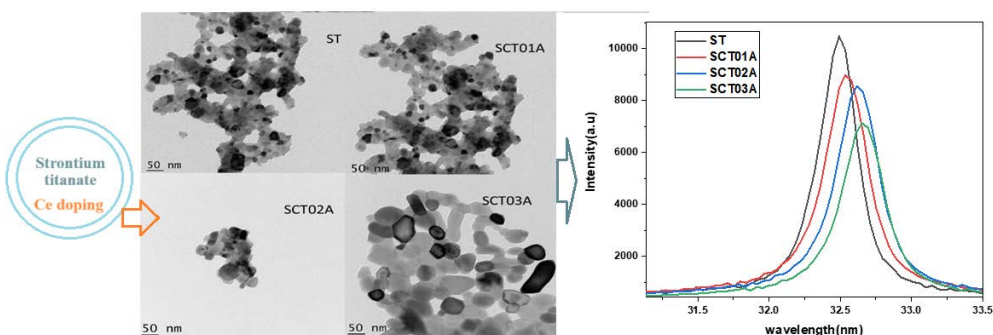
Keywords: Perovskites, W-H plot, combustion method, Urbach energy, dye-sensitized solar cells

INTRODUCTION

It has taken more than 150 years to completely understand the physical characteristics of perovskites since Gustav Rose identified the basic perovskite calcium titanate ($CaTiO_3$) in the Ural Mountains.[1] The perovskite compounds possess a framework having the form ABX_3, whereby the cations A and B have distinct dimensions while the anion X is attached to both of them. The A and B locations in the perovskite can be inhabited by any kind of metal as well as semimetal from the periodic table of elements. Although this can be any ion at this point, the anion has always been oxygen. The incredibly versatile geometrical features of the aforementioned substance enable them to display an extensive range of electrical and magnetic behavior. They are widely used in a wide variety of disciplinary fields.[2] Since they serve to eliminate contaminants from vapor mixtures in a selective way, these substances are referred to as cleansing accelerators. Furthermore, perovskite materials catalyze oxygen formation and oxygen reduction reactions, which have applications in the electrolysis of water, fuel cells, rechargeable batteries, and in the synthesis of organic compounds.[3] Perovskite materials can additionally be

*Corresponding Author: Dr. Jijimon K Thomas
Email: jkthomasemrl@yahoo.com

Journal of Integrated Science and Technology

J. Integr. Sci. Technol., 2024, 12(4), 781   Pg 1

employed as cathodes in solid oxide fuel cells.[4] These kinds of compounds additionally serve as suitable materials for situations involving gas detection. Several investigations on perovskites have been carried out in various areas of biological sensors.[5,6] Numerous research studies have employed perovskite as a neurotransmitter sensor. The investigation of fuel cells and solar cells took advantage of the perovskite materials. The uses of metal halide perovskites in optoelectronics and photovoltaics are widely understood.[7] Due to their unique tunable properties, perovskite compounds have significance in the hunt for feasible energy materials for energy harvesting devices.[8,9] Perovskite materials are also advantageous for thermoelectric uses, which use heat to generate power.[10] The static dielectric constant ε_0 of the material eventually decides the extent to which capacitive storage devices, especially static and dynamic random-access memories, can be miniaturized. Perovskites are frequently utilized in such technical applications and have high values for ε_0.[11]

Strontium titanate is an exemplary electroceramic as well as one of the most deeply studied oxide materials. $SrTiO_3$ (STO), having a cubic-perovskite type architecture exhibiting a band gap of 3.2 eV and outstanding chemical stability, has served as a common template to facilitate the epitaxial development of a variety of perovskite oxides having a broad spectrum of traits.[12] It adopts the cubic perovskite structure and crystallizes in the Pm3m space group.[13] Strontium titanate ($SrTiO_3$) represents one of the oxides that has been investigated in the ABO_3 perovskite-type frameworks owing to its tremendous industrial significance. Heterostructures produced from $SrTiO_3$ have been frequently coupled with various oxides for a variety of applications. Such heterostructures demonstrate amazing attributes involving thermoelectricity in addition to superconductivity. It even turns into a superconductor itself at extremely high electron densities (which is generated through doping or processing at a highly reducing atmosphere), though only when reaching temperatures as low as 0.4 K.[14] Due to quantum fluctuations, $SrTiO_3$ does not change into a ferroelectric phase, but its high dielectric permittivity at ambient temperature (about 300) is utilized in several electroceramic applications.[15] In field-effect transistors and DRAM memory devices, strontium titanate-based materials are proposed as an alternative high-permittivity dielectric material.[16]

Renewable energy from the sun can be utilized to produce power through photovoltaic cells, which is an environment-friendly approach to generating power. Dye-sensitized solar cells (DSSC), which were initially created by Gratzel et al. in 1991 and have drawn a great deal of interest in the preceding couple of centuries, are considered to be among the most promising ways of energy conversion.[17] The two electrodes that comprise a cell are the counter electrode and the photoanode. The most common substrates are glasses coated with transparent conductive oxide (TCO) or fluorine-doped tin oxide (FTO), which are subsequently painted with titanium dioxide (TiO_2) nanoparticles.[18] The TiO_2-coated substrate acts as a photosensitizer to form a photo anode by enabling the molecules of dye to absorb in. The area that lies between the electrodes is filled with an electrolyte, and a sealing layer additionally exists there. Furthermore, a layer of platinum/graphite has been applied on the counter electrode in the DSSC.[19]

This article outlines the construction and characterization of standard DSSCs, which consist of a platinum counter electrode, an electrolyte solution based on the iodide/iodine redox pair (I-/I-$_3$), a photoanode with either Ce-doped strontium titanate coating that has been dyed by a natural sensitizer or a nanocrystalline strontium titanate coating dyed by a natural dye. Here, we also go through the structural, optical, and electrical properties of doped and pure strontium titanate.

EXPERIMENTAL TECHNIQUES

Material preparation

Materials bearing the structure $Sr_{(1-x)}Ce_xTiO_3$ (x=0,0.01,0.02,0.03) have been developed using a single-step burning procedure. To make a transparent solution devoid of any kind of precipitation, strontium nitrate, and cerium (III) nitrate hexahydrate were dissolved in distilled water, and titanium (IV) isopropoxide was mixed with ethanol. After that, citric acid was introduced to the titanium (IV) isopropoxide solution. The quantity of citric acid was determined by the overall valence of the oxidizing and reducing substances to obtain the greatest generation of energy upon burning. The percentage of cations to citric acid was kept stable at 1:1. The initial solution has been generated via the combination of all of the solutions mentioned above. A solution of ammonia was added to it to serve as fuel. The starting point solution was then treated with strong nitric acid. The proportion of oxidant to fuel was modified by the incorporation of water-based ammonia. On a hotplate, the mixture was warmed to an ultimate temperature of 250℃. A foam-like substance appears as the outcome of the preliminary complex getting dehydrated, which leads to uniform expansion. Burning of the foam created the requisite nanoparticles, which were a fluffy white powder. In the current one-stage ignition procedure, citric acid serves as a component of complexing instead of polyvinyl alcohol and ammonia instead of urea. Ceramic items are frequently produced at relatively elevated temperatures. This alteration of the complexing agent and oxidant fuel combination allows the basic combustion process itself to yield one-phase, nanoparticles at exceptionally low temperatures.[20,21] Materials for x=0,0.01,0.02, and 0.03 were assigned the labels ST, SCT01A, SCT02A, and SCT03A, respectively

Pellet preparation for impedance spectroscopic research

Dense solid ceramic pellets formed from burning leftovers were utilized to conduct the impedance measures in this research. Each pellet was of a stable dimension of two millimeters and an outer diameter of approximately ten millimeters. Nanoceramics were grounded in a five percent polyvinyl alcohol mixture with an agate crusher and pestle before being unilaterally pressed at an applied pressure of twenty mega Pascals. The resulting pellets were subsequently heated for three hours at an approximate temperature of 1350 ℃ to solidify them till they accomplished ninety-five percent to ninety-eight percent of their predicted densities.[22] An LCR meter was utilized to gauge the impedance of the bulk ceramics from fifty hertz and five megahertz (MHz). At an initial bias voltage of 1 V with an excitation voltage that varied between 0.8 to 1 mV, impedance studies were conducted.

Journal of Integrated Science and Technology

J. Integr. Sci. Technol., 2024, 12(4), 781   Pg 2

Construction of solar cell

Employing the aforementioned synthesized samples, we carried out the following procedures to build solar cells with dye sensitization. The resulting ceramic samples were smoothed out and combined in a precise ratio with ethanol and triton X 100 to formulate a paste out of them. The even mixture was subsequently applied using the doctor blade technique to the conducting surface of a glass sheet layered with fluorine tin oxide (Solaronix, Switzerland).[23,24] The aforementioned sample-coated photoanodes underwent a 30-minute 450°C muffle furnace drying procedure after being dried in the air initially. Some amount of dried and crushed henna plant leaves (See image 1) was employed to produce the dye solution. The powdered leaves were subsequently dissolved with ethanol, placed aside for twenty-four hours, and strained before it was utilized as a sensitizing solution. To sensitize the photoanodes, it was placed in the filtrated extract for twenty-four hours. A redox (I-/I3-) electrolyte mix (Mosalyte TDE-025, Solaronix, Switzerland) was inserted between this photoanode and a second electrode that was platinum-coated to assemble a photovoltaic cell.

Figure 1. Picture of henna plant leaf

The counter electrode was fabricated from a piece of fluorine tin oxide (FTO) covered glass that was coated with Platisol T (Solaronix, Switzerland). It was subsequently heated for thirty minutes at 450 degrees Celsius in a muffle furnace for its use in the solar cell.

Methods of Characterization

The patterns of XRD have been captured by employing a diffractometer for X-rays (Bruker D8 Advance) employing nickel-filtered Cu K α rays. An ultraviolet-visible spectrophotometer (Perkin Elmer Lambda 365) was deployed to capture entire UV-Vis-DRS traits in the 200-800 nm spectrum in ambient conditions. Transmission Electron Microscopy (TEM, Jeol/JEM 2100) at 200 kV has been utilized to analyze the particulate matter traits of the combustion product. A Thermo Nicolet Nexus IS50 spectrophotometer was applied to gather FT-IR spectra with wavelengths within 4000 cm^{-1} and 400 cm^{-1}. The electrical properties of the designed photovoltaic cells were evaluated via a solar simulator and a Keithley source meter having a source voltage of 100 mW/cm^2. An impedance tester (LCR HiTester 3532e50,

Hioki, Japan) was put to use to perform the impedance spectroscopic investigation of the sintered pellets.

RESULTS AND DISCUSSION

Images 2 and 3 demonstrate the XRD pattern and peak displacement detected in the XRD images of the produced nanoceramics. Cubic structures have been observed to exist in every specimen, lacking the sign of contaminant components. The (100), (110), (111), (200), (210), (211), (220), (300), and (310) planes of cubic SrTiO$_3$ crystals can be utilized to describe the pattern of diffraction. The material having cerium doping displayed an XRD pattern alteration, with peaks migrating to higher two-theta values. Since cerium and strontium ions possess distinct ionic radii, this may happen. The unit cell parameters decreased for the doped sample. This is because the ionic radius of strontium is greater (r$_{Sr}^{2+}$ = 113pm) than the ionic radius of cerium (r$_{Ce}^{4+}$ = 92pm). The XRD pattern displayed no additional features at all. This indicates that the phase the development was completed during the burning process itself .[25] The mean size of the crystallite for both strontium titanate and cerium-doped strontium titanate- specimens has been calculated using the Scherer formula.
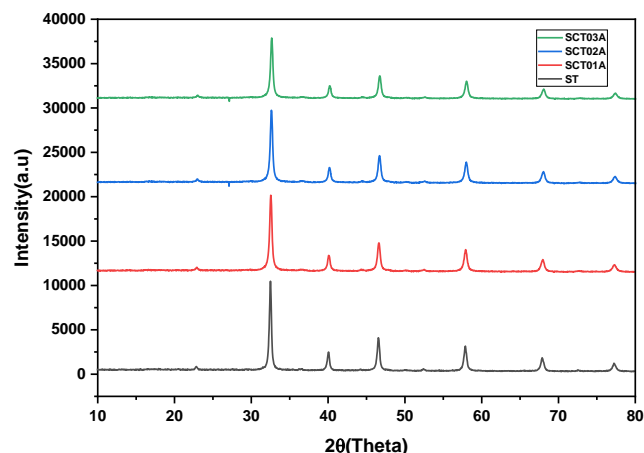
Figure 2. XRD pattern of the samples
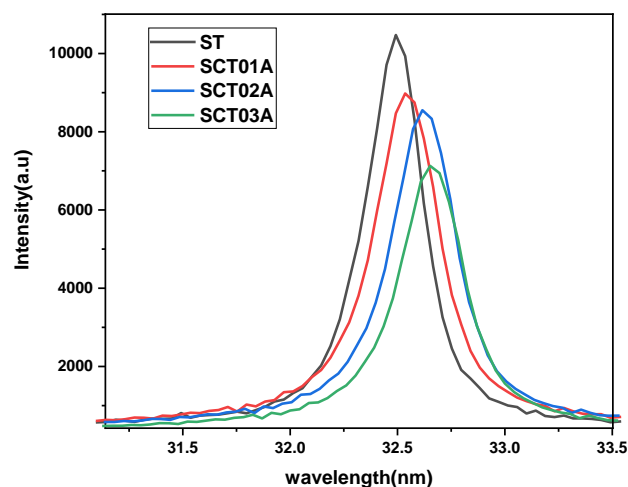
Figure 3. Illustration of the peak shifting observed in the XRD of the samples

Journal of Integrated Science and Technology

J. Integr. Sci. Technol., 2024, 12(4), 781   Pg 3

The following is the Scherer formula[26]

$$D = \frac{k\lambda}{\beta \cos\theta} \qquad (1)$$

where β stands for full width at half maximum (FWHM), k is a constant, λ is the X-ray wavelength, and θ is the diffraction angle. As the cerium content in strontium titanate increased, so did the crystallite size.[27] Since all of the cerium atoms fit inside the crystal structure of strontium titanate, the expansion of the crystallite will not be hampered by the inclusion of cerium at the A site of the perovskite matrix. Hence the crystallite size increased with an increase in cerium concentration.

Macrostrains in the samples were determined with the modified W-H equation utilizing uniform deformation mode (UDM). The uniform deformation model (UDM) accounts for the uniform strain imposed by imperfections in crystals in nanocrystals throughout the crystalline axis. In a nutshell, the strain, which is an isotropic phenomenon, is interpreted under UDM. Such inherent strain leads to the natural widening within the diffraction profile, thus this deformation-induced peak widening is described as

$$\boldsymbol{\beta sin\theta = 4\varepsilon tan\theta} \qquad (2)$$

In light of this, it is possible to express the total widening brought on by strain and size at a particular peak with the (hkl)value as

$$\beta = \beta_{size} + \beta_{strain} \qquad (3)$$

where, for various diffraction planes, β_{hkl} is the full width at half of the maximum intensity and it was given by

$$\beta = \frac{k\lambda}{DCos\theta} + 4\varepsilon tan\theta \qquad (4)$$

when we rearrange the formula above, we obtain

$$\beta Cos\theta = \frac{k\lambda}{D} + 4\varepsilon Sin\theta \qquad (5)$$

Here ε is the microstrain, D is the crystallite size and θ is the angle of diffraction. Equation (5) is a linear formula that accounts
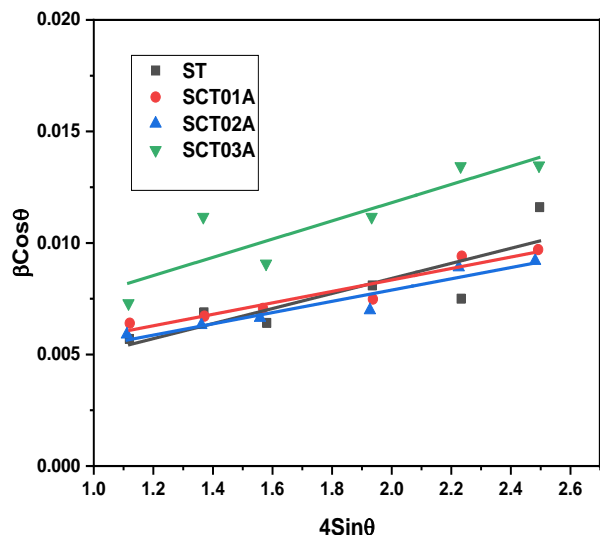
Figure 4. W-H plot of the samples

for the isotropic nature of the crystal and may be referred to as the Uniform deformation model (UDM) formula. Figure 4 shows a representation of this formula (Williamson-Hall plots), where each diffraction peak is symbolized by a term (4Sinθ) along the X-axis and (β Cosθ) along the Y-axis. The gradient of the line reveals the inherent strain value, whereas the intercept of the straight line gives the mean size of the particles of the nanocrystals. The origin of the lattice strain is primarily attributable to the structural expansion or contraction in nanocrystals resulting from dimension confinement owing to the small deviation in the arrangement of atoms.[28,29]

Table I. Measurements obtained from the XRD pattern

Parameters	ST	SCT01A	SCT02A	SCT03A
Lattice parameter (A^0)	3.8912	3.8711	3.8688	3.8432
The volume of the unit cell ($A^{0\,3}$)	58.9183	58.0100	57.9067	56.76
Crystallite size(nm)	19.10	20.68	22.22	22.76
Micro strain	0.00338	0.00257	0.00267	0.00411

Morphological Analysis
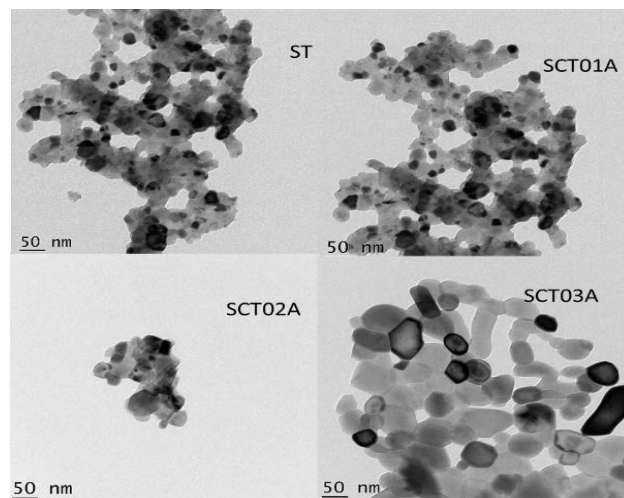
Figure 5. HRTEM pictures of the prepared nanoceramics

Figure 5 displays the HRTEM picture of the generated nanoceramics. The size, crystal structure, and defects of the material are all discernible from the TEM image. By using this information one can comprehend the properties and behaviour of the material better and the performance of the material in various applications may be enhanced. The ST nanoparticles are virtually spherical and have a diameter that ranges from 18 to 20 nm, according to the TEM picture. For both doped and undoped materials, the particle size is in good agreement with the estimated value from the Debye-Scherer formula. The crystallite size enhanced for the doped samples, which is evident in the TEM pictures. The images make it readily obvious that doping with

Journal of Integrated Science and Technology

J. Integr. Sci. Technol., 2024, 12(4), 781   Pg 4

cerium caused the size of the crystallites in strontium titanate to increase.

FTIR-spectrum analysis

Figure 6 shows the Fourier transform infrared spectra of the manufactured materials. The metal-oxygen (O-M-O) stretching motions at the B-site cause the transmittance band in ABO_3 perovskite that is often seen in the 450–650 cm^{-1} wavenumber area. This band, which is associated with the stretching vibrations of the Ti-O bond, confirms the blue shift brought on by the doping concentration of Ce ions in the present lattice. The absorption peak, that is centred between 1426 and 1492 cm^{-1}, indicates the process that occurred when the molecules of absorbed water (H_2O) were deformed.[30]
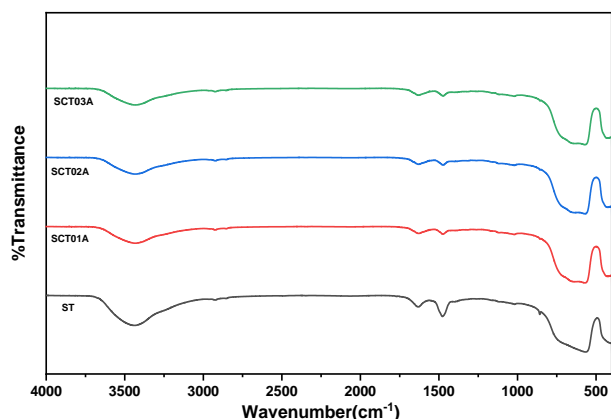
Figure 6. FTIR spectra of the samples

UV-Visible spectroscopic studies

a UV-Visible absorption spectra
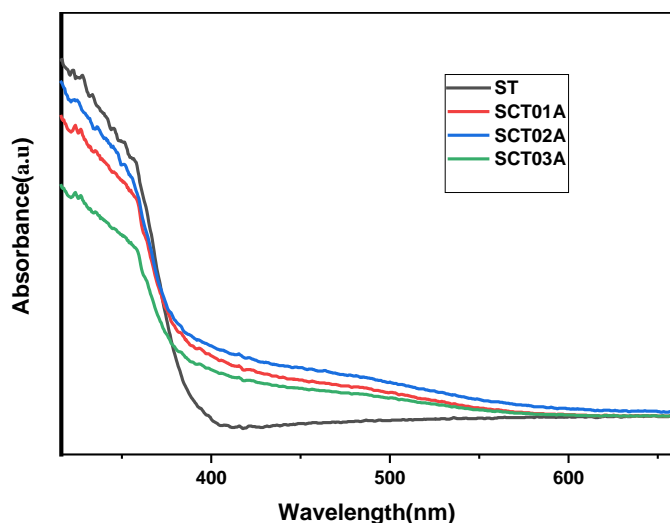
Figure 7. UV-visible absorption spectra of the nanoceramics

An in-depth analysis of the optical attributes of a material is essential to comprehend its potential application in photovoltaic and optoelectronic systems. Figure 7 displays the UV-visible absorption patterns of the synthesized material. The absorption bands of the doped materials revealed an upsurge in the absorption of light in the visible part. As a result, the optical bandgap of doped nanostructured ceramics narrowed, enhancing the level of visible light absorption in doped samples. The optical bandgap of the doped nanostructured materials material dropped as a consequence of the creation of additional localized states and flaws in the host matrix brought about by the intrusion of Ce ions.

b Determination of the bandgap

A method for estimating the band gap using optical absorbance data was suggested by Tauc et al. after studying the optical and electrical characteristics of amorphous germanium. Davis and Mott's research in amorphous semiconductors[31] indicates that the discrepancy between photon energy and band gap affects optical absorption intensity as follows:

$$(\alpha h\upsilon)^{\frac{1}{n}} = B(h\upsilon - E_g) \qquad (6)$$

Whichever is the kind of electronic shift that gives rise to the absorption, n could correspond to 1/2, 3/2, 2, or 3. The sixth equation also refers to the Planck constant h, photon frequency (h υ = 1240/wavelength), absorption factor α, parameter B about the effective masses corresponding to each of the bands, and band gap energy E_g. The n proportion for materials with a straight band gap is 1/2, whereas the same for materials with an indirect band gap is 2. To properly conduct a Tauc's inquiry, it is crucial to first acquire optical absorbance information for the sample under study that covers a broad spectrum of values from below the band-gap transition to above it [32].
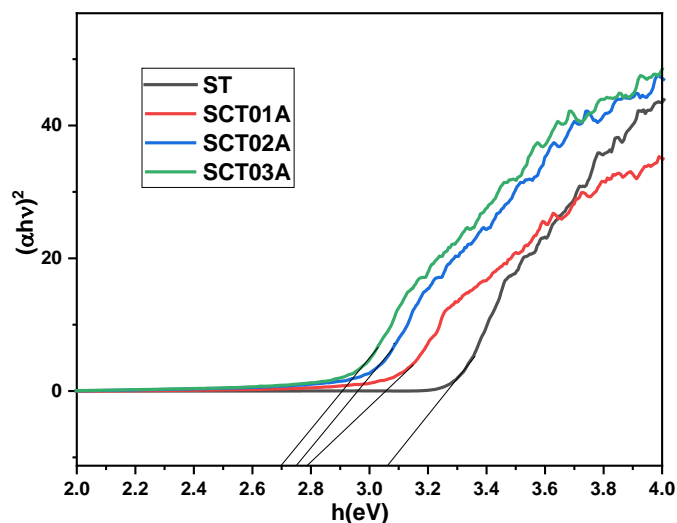
Figure 8. Tauc plot of the samples

Figure 8 depicts the Tauc plot of the sample. The band gap data determined via the Tauc plot are given in Table 2. As doping increased, the bandgap of the samples diminished. When cerium atoms were added to strontium titanite, significant flaws in the substance developed because Ce and Ti had distinct ionic radii. The strontium titanate bandgap was reduced due to structural aberrations brought on by doping.

c Calculation of Urbach energy

The Urbach energy may give an understanding of the effects of disarray in amorphous or crystalline systems. The tailing of the density of states is associated with the lack of far-reaching order in glassy/amorphous materials. It is also feasible to forecast the band architecture as well as the band gap energy in crystalline and amorphous substances by looking at optical absorption data. In optical absorption, an absorption fringe having an exponentially expanding absorption factor α is left there whenever a photon possessing energy higher than the band gap is absorbed. By the following relation, the increase in α is connected to the energy hυ.

$$\alpha = \alpha_0 e^{\frac{h\upsilon}{E_u}} \qquad (7)$$

Here E_u is the Urbach energy and α_0 is a constant. E_u has been calculated using the reverse of the gradient of the Urbach's graph (See Figure 9) within the territory of low photon energies [33]. The findings suggest the optical bandgap estimates have somewhat declined as a result of the expanded irregularity imposed by doping. Therefore, the decline in bandgap may be an outcome of structural alterations driven by the incorporation of dopants into the material. Consequently, it is possible to assert that the optical bandgap relies on the composition of the material.[34]
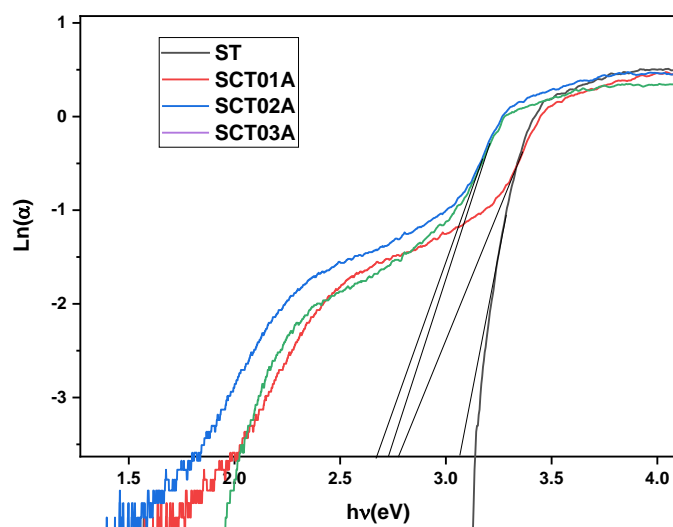
Figure 9. Ln(α) variation relative to the energy of photons

Table II. The characteristics derived from UV-visible absorption spectra

Ceramic material	Bandgap(eV)	Urbach energy(eV)
ST	3.17	0.550
SCT01A	2.78	0.694
SCT02A	2.75	0.711
SCT03A	2.69	0.734

Thus, the bandgap decreased and Urbach energy increased with the doping of cerium in strontium titanate.

Dielectric constant and loss tangent

The dielectric examination technique is frequently utilized to systematically assess structure, boundaries of grains, transport capabilities, and potential for charge retention of materials. The value of the dielectric constant serves as a gauge for the extent to which an electrical field impacts a material medium.[35] A material undergoes a wide range of molecular polarisations primarily as an outcome of the applied field.[36–40] In both pure and cerium-doped SrTiO$_3$ ceramic samples, diagram 10 demonstrates the link between frequency values and the dielectric constant fluctuation, measured at room temperature. The mathematical equation beneath has been applied to figure out the dielectric value of the material.

$$\varepsilon = \frac{C_p d}{\varepsilon_0 A} \qquad (8)$$
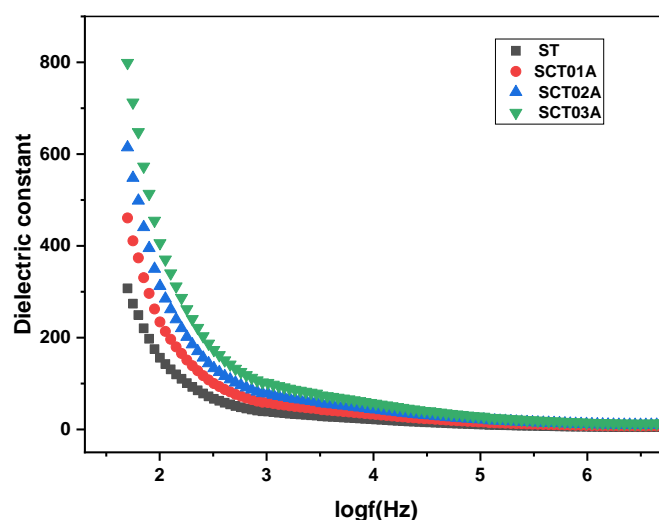
Figure 10. The change of the dielectric constant values with log frequency

Here A indicates the area of the cross-section in millimeters, d is the measurement of thickness in millimeters, C_p is the capacitance expressed in farads, and ε_0 is the permittivity of space. Figure 10 shows an elevated dielectric constant value in the low-frequency spectrum. The development of mild phonon oscillations within TiO$_6$ bonds could be an explanation for this behavior. When frequency rises to an elevated quantity, the dielectric constant drops. Diverse polarisation mechanisms have been taking place inside the material, which is the reason that the low-frequency spectrum possesses an elevated dielectric value. Within the upper frequencies, the value of the dielectric constant gets invariant with frequency. When the frequency rises, the ionic, dipolar, as well as space charge polarisation becomes incapable of keeping up with this quickly changing frequency, allowing the dielectric constant to evolve unrelated to the frequency in the region of high frequencies. According to previously reported findings, the cerium doping at the A and B positions in the perovskite strontium titanate brings about different modifications to the dielectric characteristics.[41] The A location of strontium titanate could be cerium-doped to raise its dielectric constant, as reported by J. Qi et al.[41] On the other hand,

Vedika et al.[42] reported that the dielectric strength of strontium titanate that had undergone cerium B site doping decreased.[42] It is well-established that the dielectric constant at microwave frequencies is significantly impacted by the relative density, secondary phases, and ionic polarizability. The impact of relative density in the dielectric constant becomes less noticeable when the objects being studied have relative densities that are above 96 percent of their predicted density. Owing to the lack of secondary phases in the patterns generated by XRD, its effect may have also gone ignored. Therefore, the factor that contributes to the increase in dielectric constant is ionic polarizability. Sr^{2+} [4.24 $(A^0)^3$] rates favorably to $(Ce)^{4+}$ [3.94$(A^0)^3$] in terms of ionic polarizability. Thus, it is predicted that the dielectric constant would decrease due to this change in ionic polarizability with doping. But dielectric constant increased with cerium doping. It is clear from the XRD pattern that crystallite size increased with an increase in cerium concentration. Thus, the grain boundaries decrease and the resistance decreases. This decrease in resistance has been proved experimentally by impedance spectroscopic methods and is given in the sections below. This decrease in resistance values allows smooth movement of charges within the lattice. Thus the dielectric constant values increase with the increase in cerium doping at the A site of the perovskite structure.[43–45]
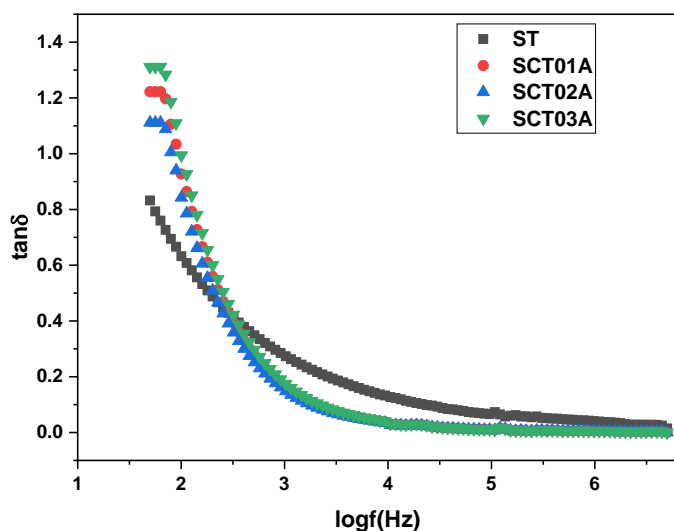
Figure 11. Dependence dielectric loss with log frequency at ambient temperature

The dissipation of energy of material in the dielectric system, whose value is proportionate with the imaginary part of the dielectric constant, is the physical importance of the dielectric loss. Figure 11 indicates the loss in the material. It is demonstrated that at low frequencies, the loss tangent rapidly falls for all samples, but that at higher frequencies, it becomes frequency invariant. By the phenomenological concepts given out by Maxwell, Wagner, and Koop, the change can potentially be interpreted in the framework of space charge polarisation. Space charges can track the frequency of the field at low ranges. However, they could fail to have sufficient time to collect and relax at elevated frequencies. Domain wall resonance, which has been muffled, is another factor

contributing to this loss component [46]. Furthermore, the dielectric loss tangent of the doped sample is large in the low-frequency area and low in the high-frequency zone.

Electrical behaviours

Through analyzing the AC electrical conductivity, it is able to acquire essential information regarding the imperfection level that occurs in the gap of semiconductor materials. The hooping motions of carriers of charges in materials may be studied using the frequency-dependent electrical conductivity investigation. At ambient temperature and 800^0 C, the two figures 12 and 13 illustrate the electrical conductivity of pure and cerium-doped $SrTiO_3$ samples as a function of frequency. The high-frequency zone exhibited a spike in electrical conductivity. The accessibility of the material to extra charge carriers and conduction regions is accountable for this.
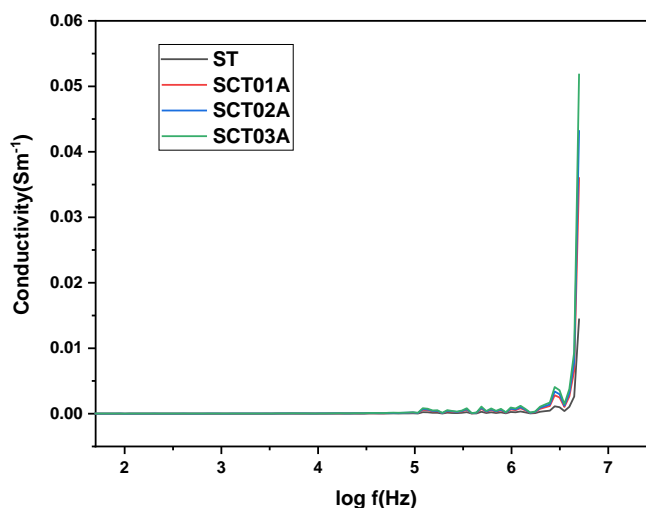
Figure 12. Electrical conductivity of bulk ceramics measured at ambient temperature with log frequency

It is also feasible to separate the conductivity spectrum into two halves. The low-frequency conductivity, sometimes referred to as so-called DC conductivity, was illustrated in the first section. The conductivity of alternating current (AC), which increases with frequency, was assumed to be the source of the second component. By Koop's theoretical terms, the high-frequency region's dispersion, which is brought on by both exceptionally conductive grains and excessively resistive grain borders, is represented by the AC conductivity.[47] The improved hopping of the charge carrier mechanism may be the cause of the higher grain conductivity at high frequencies. In the meantime, a greater likelihood of charge carriers tunneling might be the cause why there is enhanced conductivity at elevated temperatures.

As a whole, frequency dependency of the conductivity complied with Jonscher's power law[48].

$$\sigma(\omega) = \sigma_{dc} + A\omega^s \qquad (9)$$

Where σ_{dc} is the DC conductivity, ω is the observed angular frequency, and s is a temperature-dependent parameter. A is a parameter that controls the strength of the polarisation and is greatly impacted by the composition and temperature of the sample.

Journal of Integrated Science and Technology

J. Integr. Sci. Technol., 2024, 12(4), 781   Pg 7

Overall, the second part on the right side of Jonscher's power-law equation indicates the frequency-dependent (AC) conductivity. The two figures 12 and 13 illustrate the way the total electrical conductivity in the produced materials increased as temperature rose.
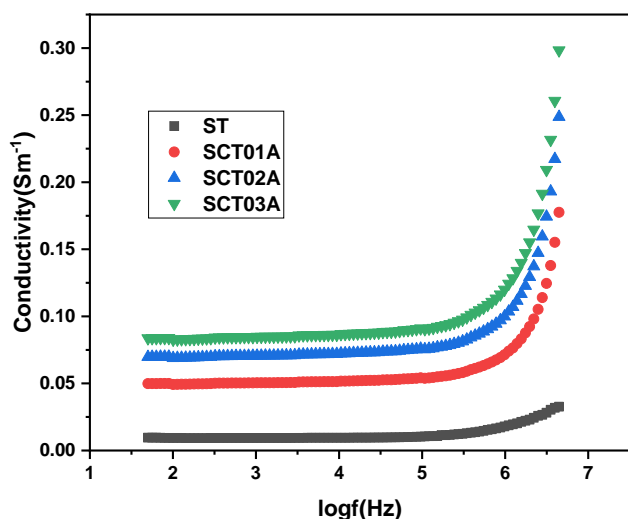
Figure 13 Bulk ceramics' electrical conductivity shown against log frequency at 800^0C
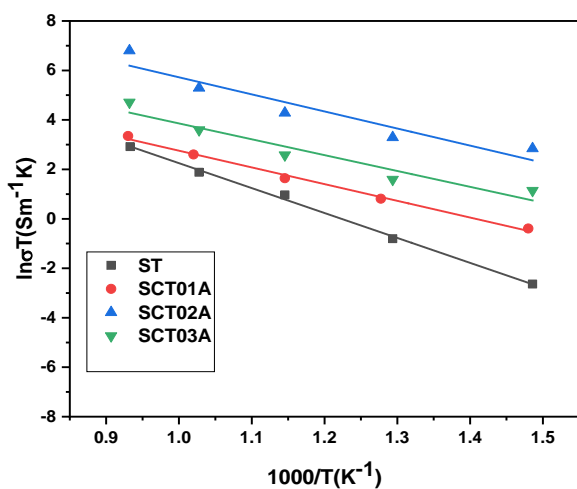
Figure 14. Arrhenius curve of the nanoceramics

Figure 14 shows the Arrhenius plot of the materials. The connection between temperature and conductivity is described by the Arrhenius law of ionic conduction, which is as follows:

$$\sigma = \sigma_0 \exp(\frac{-E_a}{K_B T}) \qquad (10)$$

E_a represents the activation energy, σ_0 represents the pre-exponential number, K_B is the Boltzmann constant, T is the absolute temperature, and σ represents the total electrical conductivity of the samples. The charge carriers in the bulk ceramics experience activation by heat, as demonstrated via the linear behavior of the ln (σ.T) against 1000/T. The slope from these graphs can be utilized to calculate the activation energy (E_a), which corresponds to the value of energy required to trigger the thermally stimulated

transport of charge carriers within the lattice. The numerical value of the pre-exponential number (σ_0) denotes the total amount of charge carriers that are found in the substance being examined. The σ_0 as well as E_a figures for the bulk have been provided in Table three. Throughout the charge transit process, charge carriers often traverse a potential wall or well to move from a constrained or localized state to a dynamic mode [49]. In strontium titanate, doping increased electrical conductivity. The activation energy in strontium titanate was decreased by doping. Thus the electrical conductivity of the doped samples has risen.[50]

Table III. Values of activation energy, pre-exponential term, and the value of electrical conductivity of the synthesized nanoceramics.

Ceramic material	Activation energy(eV)	Pre-exponential term	Conductivity(S/m) at 800^{0}C and at 1MHz
ST	0.87	2.3 x 10^5	1.6 x10^{-2}
SCT01A	0.56	1.34 x 10^4	7.1 x 10^{-2}
SCT02A	0.59	3.02 x 10^5	1.02 x10^{-1}
SCT03A	0.55	2.87 x 10^4	1.2 x 10^{-1}
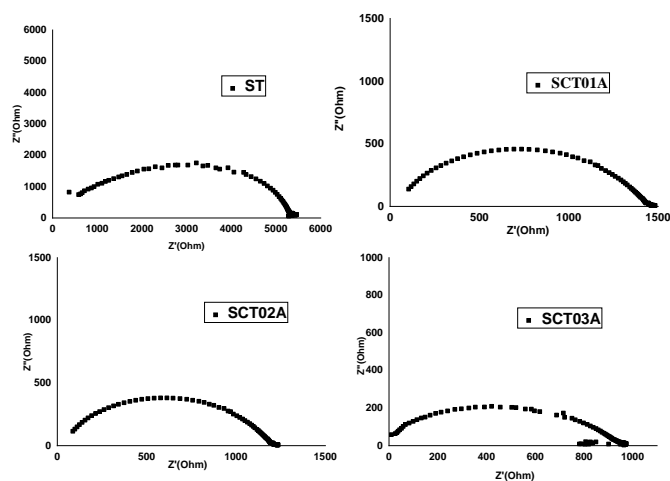
Figure 15. The plot of the real part of impedance against the imaginary part of the nanoceramics at 800 ℃

The complex impedance spectra were employed to investigate how the material behaves electrically. In the Cole-Cole diagram of bulk ceramics, there usually appear three semicircles: one in high frequency (left), another in intermediate frequency (middle), and a third in lower frequencies (right). Each of the aforementioned half-circles signifies the parts from the grain, the impact from the grain borders, plus the relationship that occurs with the electrode material. Figure 15 depicts the impedance curves for the bulk materials used in the present study. It displays a small, enormously depressed semicircle with a curving spike.[51] The low-frequency spike conveys the interaction between the conducting material of the electrode and the material being examined, and the large semi-circle portrays the union of two smaller semi-circles which stand for the grain and grain border impacts.[52] According to data analysis from the literature, if doping had been performed in the B the location of the sample, the impedance would go up. Since the ionic radii of cerium and titanium ions differ (cerium ions have higher

Journal of Integrated Science and Technology

J. Integr. Sci. Technol., 2024, 12(4), 781 Pg 8

ionic radii than titanium ions), cerium doping may hinder grain growth. As a result, only certain cerium ions can penetrate the lattice framework and some cerium ions may thus reside at the grain borders and hinder the further formation of the grains. Thus, grain growth declines with the doping of cerium at the B site.[48] By shrinking crystallite size and enlarging grain borders, cerium doping retarded the transition between states and grains. Cerium ions accumulate at the grain boundaries as doping levels rise, decrease the grain size, increase the grain boundaries, and increase the resistance. But for the A site doped sample, the ionic radii of cerium is less than that of strontium, all the cerium atoms can go inside the lattice. Thus, the crystallite size increased with the doping of cerium at the A site. Thus, grain boundaries decrease and thus, the electrical conductivity increases with the doping of cerium at the A site of strontium titanate.

The current-voltage characteristics of solar cells
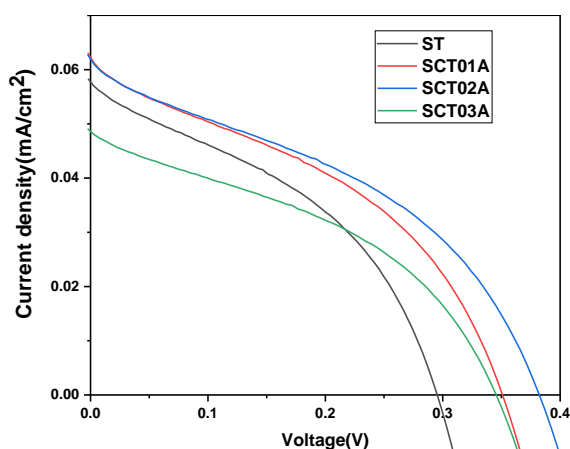
Figure 17. Current-voltage characteristics of the constructed DSSC

A glass substrate, transparent conducting layer, photoanode, dyes, electrolyte, and counter electrode topped with a sealing gasket are the different layers of components that comprise the DSSC. A small layer of transparent conducting substance has been added on top of the glass substrate, allowing sunlight to enter the cell and to carry electrons to the outside circuit. Fluorine tin oxide (FTO) or In-doped Tin oxide (ITO) or Aluminum-doped Zinc Oxide (AZO) are the substrates commonly used for transparent conducting layers. The photoanode material should be highly photosensitive, structurally stable under solar radiation and in solutions, and inexpensive. Because organic dyes have a donor-acceptor structure known as a push-pull architecture, short-circuit current density may be increased by increasing the absorption in the red and infrared areas. I^-/I_3^- is the most often utilized electrolyte in organic solvents like acetonitrile. Pt is the most commonly used counter electrode. Carbon, graphene, etc. can also be used as counter electrodes in DSSC. In DSSC, the light-absorbing dye encounters the initial photoexcitation. The nonporous photoanode's conduction band is now filled with excited electrons and is located underneath the dye's excited state. The nano-porous semiconductor supports dye sensitizers and functions as an electrical conductor. Next, the dye oxidizes. These injected electrons flow in the direction of the back

contact by passing over the photoanode nanoparticles. Through the external circuit, these electrons subsequently make their way to the counter electrode. Electrons from the ion redox mediator are absorbed by the counter electrode, where they cause I^- to be oxidized there to I_3^-, resulting in dye renewal.[53]

Using short circuit current (J_{SC}), open circuit voltage (V_{OC}), overall efficiency [η%], and fill factor [FF], one can assess the performance of a dye-sensitized solar cell at a constant light level exposure. V_{OC} (V) is the difference between the conduction band energy of a semiconducting material and the redox potential of the electrolyte, or simply the voltage across the negative and positive electrodes when the circuit is open and there is no current flowing.

Table IV. Photovoltaic attributes of DSSC using cerium-doped strontium titanate photoanodes and pure strontium titanate photoanodes

Sample	ST	SCT01A	SCT02A	SCT03A
Open circuit voltage(V)	0.2951	0.34	0.38	0.34
Short circuit current (mA/cm²)	0.0576	0.061	0.062	0.048
Fill factor	0.39	0.40	0.40	0.39
Efficiency	0.0063	0.0082	0.0094	0.0064
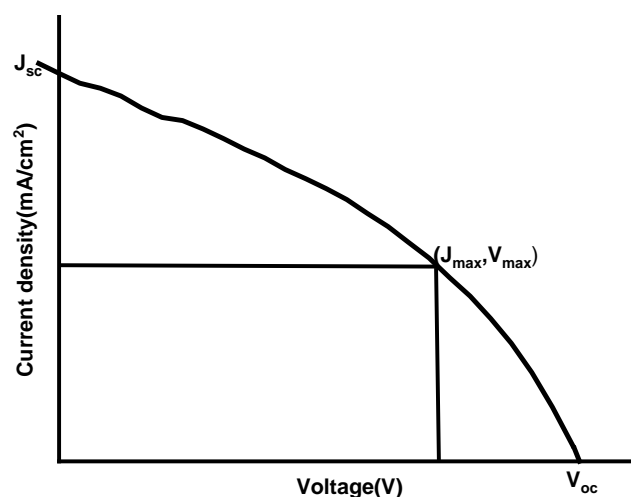
Figure 16. I-V curve to assess the efficiency of the cell

The fill factor of the DSSC is given by the equation
$$FF = \frac{J_{max}\ V_{max.}}{J_{sc}\ V_{oc}} \qquad (11)$$

Additionally, the overall efficiency η (%) is the proportion of solar energy (shining on a photovoltaic device) that is converted into electrical energy and is given by equation.[54,55]
$$\eta\% = \frac{J_{sc}V_{oc}FF}{P_{in}} \qquad (12)$$

P_{in} is the input power. Other parameters used in equations 11 and 12 are illustrated in Figure 16.

Journal of Integrated Science and Technology

J. Integr. Sci. Technol., 2024, 12(4), 781   Pg 9

The current-voltage traits for the constructed DSSCs are displayed in Figure 17, and the photovoltaic values are reported in Table 4. The DSSC with SCT01A and SCT02 samples as photoanode have shown increased photocurrents. The higher electron ejection in these materials could be an explanation of the elevated photocurrents. It was found that the SCTO2A photoanode-using cell was better than others.

CONCLUSIONS

A new combustion approach was successfully applied to yield strontium titanate and strontium titanate doped by cerium at the A site of the perovskite structure. As all of the samples crystallised, it acquired a cubic structure. In the case of doped samples, the lattice parameter reduced whereas the crystallite size went up. The dimension of the crystallites obviously increased after doping with cerium, according to HRTEM images. Regarding samples which had been doped, the optical bandgap reduced. The dielectric constants and losses of all the compounds, upon dielectric characterization, was having an identical behavioural pattern: both were higher in the low-frequency region and rapidly decreased as frequency ascended until stabilising. The dielectric constant of strontium titanate went up with A-site cerium doping. Regarding the cerium-doped sample, the loss factor increased in the low-frequency region and the loss factor decreased in the high frequency region. The frequency dependance of electrical conductivity of all the materials complied with Jonscher's power law. In the doped samples, the overall electrical conductivity increased. The decrease of activation energy enhanced the electrical conductivity of the doped samples. Also for all samples the electrical conductivity increased with rising temperatures. When employing a cerium-doped material as the photoanode, the DSSC operates more efficiently than when using an undoped sample.

CONFLICT OF INTEREST

The authors declare that none of them has any conflict of interest.

REFERENCES

1. L. Chouhan, S. Ghimire, C. Subrahmanyam, T. Miyasaka, V. Biju. Synthesis, optoelectronic properties and applications of halide perovskites. *Chem. Soc. Rev.* **2020**, 49 (10), 2869–2885.
2. L.K. Ono, E.J. Juarez-Perez, Y. Qi. Progress on Perovskite Materials and Solar Cells with Mixed Cations and Halide Anions. *ACS Appl. Mater. Interfaces* **2017**, 9 (36), 30197–30246.
3. S.M. Haile. Fuel cell materials and components. *Acta Mater.* **2003**, 51 (19), 5981–6000.
4. Perovskite Oxide for Solid Oxide Fuel Cells. **2009**.
5. M. Ghasdi, H. Alamdari. CO sensitive nanocrystalline LaCoO3 perovskite sensor prepared by high energy ball milling. *Sensors Actuators, B Chem.* **2010**, 148 (2), 478–485.
6. G. Wang, J. Sun, W. Zhang, S. Jiao, B. Fang. Simultaneous determination of dopamine, uric acid and ascorbic acid with LaFeO3 nanoparticles modified electrode. *Microchim. Acta* **2009**, 164 (3–4), 357–362.
7. X. Bao, Y. Wang, Q. Zhu, et al. Efficient planar perovskite solar cells with large fill factor and excellent stability. *J. Power Sources* **2015**, 297, 53–58.
8. W. Zhang, G.E. Eperon, H.J. Snaith. Metal halide perovskites for energy applications. *Nat. Energy* **2016**, 1 (6).
9. P. Tan, M. Liu, Z. Shao, M. Ni. Recent Advances in Perovskite Oxides as Electrode Materials for Nonaqueous Lithium–Oxygen Batteries. *Adv. Energy Mater.* **2017**, 7 (13), 1–23.
10. M. Wang, S. Lin. Anisotropic and Ultralow Phonon Thermal Transport in Organic–Inorganic Hybrid Perovskites: Atomistic Insights into Solar Cell Thermal Management and Thermoelectric Energy Conversion Efficiency. *Adv. Funct. Mater.* **2016**, 26 (29), 5297–5306.
11. C.C. Homes, T. Vogt, S.M. Shapiro, S. Wakimoto, A.P. Ramirez. Optical response of high-dielectric-constant perovskite-related oxide. *Science (80-.).* **2001**, 293 (5530), 673–676.
12. J. Chen, D.J. Morrow, Y. Fu, et al. Single-Crystal Thin Films of Cesium Lead Bromide Perovskite Epitaxially Grown on Metal Oxide Perovskite (SrTiO3). *J. Am. Chem. Soc.* **2017**, 139 (38), 13525–13532.
13. R. Merkle, J. Maier. How is oxygen incorporated into oxides? A comprehensive kinetic study of a simple solid-state reaction with SrTiO3 as a model material. *Angew. Chemie - Int. Ed.* **2008**, 47 (21), 3874–3894.
14. C.S. Koonce, M.L. Cohen, J.F. Schooley, W.R. Hosler, E.R. Pfeiffer. Superconducting Transition Temperatures of Semiconducting SrTiO3. *Phys. Rev.* **1967**, 163 (2), 380–390.
15. K.A. Müller, H. Burkard. SrTiO3: An intrinsic quantum paraelectric below 4 K. *Phys. Rev. B* **1979**, 19 (7), 3593–3602.
16. A.I. Kingon, J.P. Maria, S.K. Streiffer. Alternative dielectrics to silicon dioxide for memory and logic devices. *Nature* **2000**, 406 (6799), 1032–1038.
17. D.Y.& L.B.S. Michael F. Toney, Jason N. Howard, Jocelyn Richer, Gary L. Borges, Joseph G. Gordon, Owen R. Melroy, David G. Wiesler. © 19 9 1 Nature Publishing Group 그라첼꺼. *Nature* **1994**, 368, 444–446.
18. L. Fan, S. Kang, J. Wu, et al. Quasi-solid state dye-sensitized solar cells based on polyvinylpyrrolidone with ionic liquid. *Energy Sources, Part A Recover. Util. Environ. Eff.* **2010**, 32 (16), 1559–1568.
19. S. Ananth, P. Vivek, T. Arumanayagam, P. Murugakoothan. Natural dye extract of lawsonia inermis seed as photo sensitizer for titanium dioxide based dye sensitized solar cells. *Spectrochim. Acta - Part A Mol. Biomol. Spectrosc.* **2014**, 128, 420–426.
20. J.K. Thomas, H. Padma Kumar, R. Pazhani, et al. Synthesis of strontium zirconate as nanocrystals through a single step combustion process. *Mater. Lett.* **2007**, 61 (7), 1592–1595.
21. S. Vidya, S. Solomon, J.K. Thomas. Single step combustion synthesis of nanocrystalline scheelite Ba0.5Sr0.5MoO4 for optical and LTCC applications: Its structural, optical and dielectric properties. *J. Electroceramics* **2016**, 36 (1–4), 142–149.
22. C.N. George, J.K. Thomas, R. Jose, et al. Synthesis and characterization of nanocrystalline strontium titanate through a modified combustion method and its sintering and dielectric properties. *J. Alloys Compd.* **2009**, 486 (1–2), 711–715.
23. S.A. Abrol, C. Bhargava, P.K. Sharma. Fabrication of DSSC using doctor blades method incorporating polymer electrolytes. *Mater. Res. Express* **2021**, 8 (4).
24. S. Santhaveesuk. I-SEEC 2014 Synthesis TiO 2 with doctor blade technique for dye sensitized solar cell. **2014**.
25. T. Xie, Y. Wang, C. Liu, L. Xu. New insights into sensitization mechanism of the doped ce (IV) into strontium titanate. *Materials (Basel).* **2018**, 11 (4), 1–17.
26. J.S. Revathy, N.S.C. Priya, K. Sandhya, D.N. Rajendran. Structural and optical studies of cerium doped gadolinium oxide phosphor. *Bull. Mater. Sci.* **2021**, 44 (1), 1–8.
27. J. John, S. Suresh, S. Pillai.S, R. Philip, V.P.M. Pillai. Effect of Fe doping on the structural, morphological, optical, magnetic and dielectric properties of BaSnO3. *J. Mater. Sci. Mater. Electron.* **2021**, 32 (9), 11763–11780.
28. V. Mote, Y. Purushotham, B. Dole. Williamson-Hall analysis in estimation of lattice strain in nanometer-sized ZnO particles. *J. Theor. Appl. Phys.* **2012**, 6 (1), 2–9.
29. D. Nath, F. Singh, R. Das. X-ray diffraction analysis by Williamson-Hall, Halder-Wagner and size-strain plot methods of CdSe nanoparticles- a comparative study. *Mater. Chem. Phys.* **2020**, 239 (August 2019), 122021.
30. A.M. Youssef, H.K. Farag, A. El-Kheshen, F.F. Hammad. Synthesis of Nano-Structured Strontium Titanate by Sol-Gel and Solid State Routes. *Silicon* **2018**, 10 (3), 1225–1230.

Journal of Integrated Science and Technology

J. Integr. Sci. Technol., 2024, 12(4), 781   Pg 10

31. N.F. Mott, E.A. Davis. Conduction in non-crystalline systems V. Conductivity, optical absorption and photoconductivity in amorphous semiconductors. *Philos. Mag.* **1970**, 22 (179), 903–922.

32. M.N.H. Mia, M.F. Pervez, M.K. Hossain, et al. Influence of Mg content on tailoring optical bandgap of Mg-doped ZnO thin film prepared by sol-gel method. *Results Phys.* **2017**, 7, 2683–2691.

33. B. Choudhury, B. Borah, A. Choudhury. Extending photocatalytic activity of TiO 2 nanoparticles to visible region of illumination by doping of cerium. *Photochem. Photobiol.* **2012**, 88 (2), 257–264.

34. M.A. Hassan, C.A. Hogarth. A study of the structural, electrical and optical properties of copper tellurium oxide glasses. *J. Mater. Sci.* **1988**, 23 (7), 2500–2504.

35. Z. Fu, X. Zhang, H. Zhang, et al. On the Understandings of Dielectric Constant and Its Impacts on the Photovoltaic Efficiency in Organic Solar Cells. *Chinese J. Chem.* **2021**, 39 (2), 381–390.

36. K. Sharma, S.S. Sharma, J. Ray, N.B. Chaure. Investigation of Ru-complex free Natural dye for the application of Dye Sensitized Solar Cells. *J. Integr. Sci. Technol.* **2023**, 11 (3 SE-Material Sciences and Physics), 529.

37. R. Kamble, G.M. Karve, A. Chakradeo, G. Vaidya. Optimal sizing of Battery Energy Storage System in Microgrid by using Particle Swarm Optimization Technique. *J. Integr. Sci. Technol.* **2018**, 6 (1), 6–12.

38. A. Patsha, S. Dhara, S. Chattopadhyay, K.-H. Chen, L.-C. Chen. Optoelectronic properties of single and array of 1-D III-nitride nanostructures: An approach to light-driven device and energy resourcing. *J. Mater. Nanosci.* **2018**, 5 (1), 1–22.

39. C.V. Rudrappa, S. Ganesan. Investigation of performance and stability of multilayered organometallic halide Perovskite cell. *J. Integr. Sci. Technol.* **2023**, 11 (1), 465.

40. S. Sardar, P. Kar, S.K. Pal. The Impact of Central Metal Ions in Porphyrin Functionalized ZnO/TiO2 for Enhanced Solar Energy Conversion. *J. Mater. Nanosci.* **2014**, 1 (1), 12–30.

41. J. Qi, M. Cao, Y. Chen, et al. Cerium doped strontium titanate with stable high permittivity and low dielectric loss. *J. Alloys Compd.* **2019**, 772, 1105–1112.

42. V. Yadav, H. Cheema, R.S. Maurya, et al. Study of structural, optical, dielectric, and electric properties of homovalently substituted Ce in SrTiO3 perovskite oxide. *Ionics (Kiel).* **2022**, 28 (12), 5513–5524.

43. A. Ali, M.H. Jameel, S. Uddin, et al. The effect of Ca dopant on the electrical and dielectric properties of BaTi4O9 sintered ceramics. *Materials (Basel).* **2021**, 14 (18), 1–11.

44. G.H. Chen, J.S. Chen, X.L. Kang, et al. Structural characteristics and microwave dielectric properties of In3+ and Nb5+ co-doped CaTiO3 ceramics. *J. Mater. Sci. Mater. Electron.* **2017**, 28 (8), 6301–6307.

45. R.D. Shannon. Dielectric polarizabilities of ions in oxides and fluorides. *J. Appl. Phys.* **1993**, 73 (1), 348–366.

46. A. Ahad, M.A. Taher, M.K. Das, M.Z. Rahaman, M.N.I. Khan. Effect of Y substitution on magnetic and transport properties of Ba 0 . 95 La 0 . 05 Ti 1−x Y x O 3 ceramics. *Results Phys.* **2019**, 12 (June), 1925–1932.

47. A. Radoń, D. Łukowiec, M. Kremzer, J. Mikuła, P. Włodarczyk. Electrical conduction mechanism and dielectric properties of spherical shaped Fe3O4 nanoparticles synthesized by co-precipitation method. *Materials (Basel).* **2018**, 11 (5).

48. D. Triyono, S.N. Fitria, U. Hanifah. Dielectric analysis and electrical conduction mechanism of La1−xBixFeO3ceramics. *RSC Adv.* **2020**, 10 (31), 18323–18338.

49. A.S. Das, D. Biswas. Investigation of Ac conductivity mechanism and dielectric relaxation of semiconducting neodymium-vanadate nanocomposites: Temperature and frequency dependency. *Mater. Res. Express* **2019**, 6 (7).

50. R.S. Rejith, J.K. Thomas, S. Solomon. Structural, optical and impedance spectroscopic characterizations of RE2Zr2O7 (RE = La, Y) ceramics. *Solid State Ionics* **2018**, 323 (May), 112–122.

51. S. Parashar, S. Chaudhuri, S. Singh, M. Ghoranneviss. Electrical conduction in nanoceramic PGT synthesised by high energy ball milling. *J. Theor. Appl. Phys.* **2013**, 7 (1), 26.

52. K. Verma, S. Sharma. Impedance spectroscopy and dielectric behavior in barium strontium titanate-nickel zinc ferrite composites. *Phys. Status Solidi Basic Res.* **2012**, 249 (1), 209–216.

53. K. Sharma, V. Sharma, S.S. Sharma. Dye-Sensitized Solar Cells: Fundamentals and Current Status. *Nanoscale Res. Lett.* **2018**, 13, 381.

54. B. Siwach, S. Sharma, Mohan, D. Structural, optical and morphological properties of ZnO/MWCNTs nanocomposite photoanodes for Dye Sensitized Solar Cells (DSSCs) application. *J. Integr. Sci. Technol.* **2017**, 5 (1), 1–4.

55. T.V.B. Nagaveni, K.M. Mahadevan, R. Naik, T.O.S. Kumara. Synthesis of blue light emitting 5-carboxylicacid-2-arylsubstituted benzimidazoles as photosensitizers for dye-sensitized solar cells. *J. Mater. Nanosci.* **2020**, 7 (1), 24–28.

Journal of Integrated Science and Technology

J. Integr. Sci. Technol., 2024, 12(4), 781   Pg 11